Research Article | Vol. 30, No. 25 / 5 Dec 2022 / Optics Express 45246
Optics EXPRESS

Scalable microstructured semiconductor THz pulse sources

ZOLTÁN TIBAI,[1,*] GERGŐ KRIZSÁN,[2,3] GYÖRGY TÓTH,[1] GÁBOR ALMÁSI,[1,2] GERGŐ ILLÉS,[1] LÁSZLÓ PÁLFALVI,[1,3] AND JÁNOS HEBLING[1,2,3]

[1]*Institute of Physics, University of Pécs, Pécs 7624, Hungary*
[2]*Szentágothai Research Centre, University of Pécs, Pécs, Hungary*
[3]*ELKH-PTE High-Field Terahertz Research Group, Pécs, Hungary*
[*]*tibai@fizika.ttk.pte.hu*

Abstract: In recent years several microstructured lithium niobate THz pulse source were suggested for high-energy applications. Two types of those, the reflective and the transmissive nonlinear slab are adopted here for semiconductors. These new sources are scalable both in THz energy and size. Furthermore, they can outperform the already demonstrated contact grating source in diffraction and THz generation efficiency. Compared to the lithium niobate sources, they are more feasible, thanks to the easier manufacturing and the longer pump wavelength. They can produce intense, nearly single-cycle THz pulses at higher frequencies. With 20 mJ pumping at 1.8 μm wavelength, 45 μJ THz energy, and 17 MV/cm focused peak electric field can be expected at 3 THz phase matching frequency from the transmissive nonlinear echelon slab setup consisting of a 4 mm thick structured plan-parallel gallium phosphide crystal.

1. Introduction

Intense, nearly single-cycle terahertz (THz) pulses can be used, for example, in materials science [1–5] and for the acceleration of free electrons [6,7] and protons [8]. Optical rectification of femtosecond laser pulses has become the most efficient and widely used method of intense THz pulse generation in the low- (about 0.1-2 THz) and mid-frequency (approximately 2-10 THz) part of the THz spectrum. Conventional tilted-pulse-front pumping of lithium niobate (LN) prism has been providing the highest THz pulse energies and efficiencies in the low-frequency part of the THz spectrum [9], which is especially advantageous for particle acceleration. However, this setup has substantial limitations: (i) Limited interaction length due to angular dispersion. (ii) Prism shape of the LN crystal with a large ($\gamma \approx 63°$) wedge angle. (iii) Imaging errors. Energy scalability is limited by (i-iii), while the availability of uniform THz beam is hindered by (ii) and (iii) [10–12]. Over the past few years, extensive effort has been made to reduce or even eliminate these limitations [12–18]. It has been recently demonstrated that nonlinear semiconductor materials offer a promising alternative to LN for efficient THz pulse generation [19], also enabling the construction of scalable (in THz energy and focused field) monolithic contact-grating (CG) sources [20–22]. Semiconductor materials must be pumped at an infrared wavelength sufficiently long to suppress two- and three-photon absorption to avoid the associated free-carrier absorption in the THz range. Typically, tilted-pulse-front pumping is needed in this case for phase matching [23], but the pulse-front-tilt (PFT) angle - and correspondingly the angular dispersion - is significantly smaller (~20°-25°) compared to the LN sources. The smaller angular dispersion allows the use of thicker crystals, compensating for the semiconductors' smaller effective nonlinear optical coefficient compared to LN [24].

In the case of plan-parallel CG semiconductor THz sources, the interference of two symmetrical (±1) diffraction orders limits the efficiently usable pump intensity and, correspondingly, the pump-to-THz conversion efficiency [25].

#472021 https://doi.org/10.1364/OE.472021
Journal © 2022 Received 4 Aug 2022; revised 14 Sep 2022; accepted 19 Sep 2022; published 29 Nov 2022

Optics EXPRESS

In the present paper, we recommend using the previously introduced concepts for LN [16–18] in the case of semiconductors too, which can lead to further enhancements in the implementation, diffraction efficiencies (DE), and THz conversion efficiencies compared to the CG or even to the LN cases. Moreover, these recommended setups are free from limitations (ii) and (iii) since no imaging optical element is needed and a plan parallel semiconductor slab can be used. So, they are uniformly scalable to large sizes and high pump energies without any principal limitation. Furthermore, in both recommended setups, only one diffraction order (or reflected beam) is present, allowing higher intensity pumping.

For introducing the setups, we assumed gallium phosphide (GaP) as nonlinear material (NM), 1.8 μm pump wavelength, which is longer than the three-photon absorption edge in GaP [19,26], and 3 THz phase matching frequency. However, we would like to note that these concepts can be adapted to different semiconductor NMs, pump wavelengths, and phase matching frequencies.

2. GaP RNLS and RNLS-ESR

The reflective nonlinear slab (RNLS) concept introduced in Ref. [17] proposes THz generation by pump beams diffracted in the $\pm m^{th}$ orders from a structured reflector created on the back side of the NM. Compared to the setup based on LN or lithium tantalate (LT) [17], GaP can provide higher diffraction efficiency (>90%). Furthermore, the smaller difference between the NIR and THz refractive indices of GaP and the smaller necessary PFT angle allows using an asymmetric, sawtooth-like grating profile in the case of GaP. This asymmetric grating structure diffracts the pump beam efficiently only in the $-m^{th}$ diffraction order. In this case, the optimal pump intensity is not limited by the interference of the $\pm m^{th}$ diffraction orders, which allows higher THz generation efficiency compared to the GaP CG setup. The GaP sawtooth-like grating profile and the setup is shown in Fig. 1(a). Manufacturing a grating on the back side of the NM with proper surface quality and a few-micrometer grating period can still be challenging. It is much easier to manufacture a metal profile; therefore, to introduce the necessary PFT angle, similarly to the LN (LT) case [18], the use of an external structured reflector (ESR) is suggested. For efficient coupling between the NM and ESR, a high refractive index liquid (HRIL) has to be used [17]. Here we would like to note that the RNLS-ESR setup can be easily adapted to different pump wavelengths and phase matching frequencies simply by changing the ESR. The GaP RNLS-ESR setup is shown in Fig. 1(b).

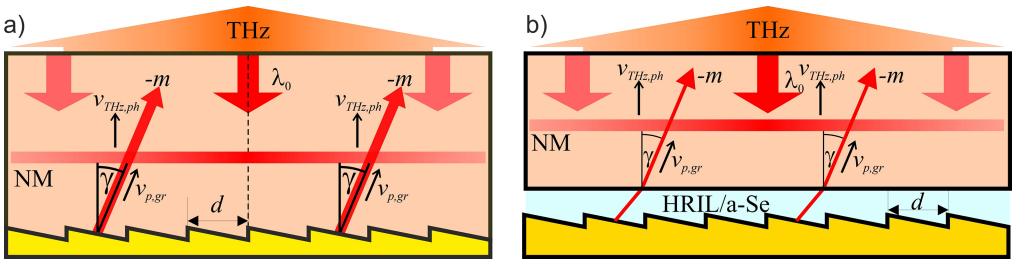

Fig. 1. (a) GaP-RNLS THz source, where the periodic structure is created on the back surface of the NM itself. (b) GaP-RNLS-ESR THz source. HRIL is used between the NM and the ESR for optical coupling.

Briefly, the working principle of this setup is the following: The pump beam incident perpendicular to the top surface of the slab (Fig. 1(b)) reaches the ESR by propagating through the NM and HRIL layers without generating any THz radiation in the lack of velocity matching. While diffracting on the ESR, an angular dispersion and correspondingly a tilted-pulse-front (see the red horizontal band in Figs. 1(a) and (b) is introduced in the backward propagating pump beam. It is evident by simple geometrical considerations that the pulse-front-tilt angle equals the

Optics EXPRESS

γ diffraction angle shown in Fig. 1, which enables the use of a plane parallel NM. The γ value required by the velocity matching can be set by the d grating period at a given diffraction order. Here, we would like to note that Fresnel reflection of the pump can be significantly reduced to a few percent at the input side by conventional anti-reflection (AR) coating (this does not affect the THz pulse). Furthermore, it is also possible to reduce both pump and THz reflection at the input (for the pump and output for the THz) side using an α-quartz plate (z-cut) [27,28] with the appropriate thickness (11.9 μm).

From the point of view of optimized optical pump-to-THz conversion, the DE of the pump beam is a crucial factor. DE (taking into account the Fresnel losses at the HRIL - NM interface) as a function of the HRIL's refractive index was determined by COMSOL simulations for a few diffraction orders. The results are shown in Fig. 2. In all cases, the DE increases with the HRIL refractive index, as is expected. For the |m|>1 cases, as obvious from the figure, the DEs are sufficiently large (>70%) even at low HRIL refractive index values. These DE values are comparable to the CG's predicted efficiencies [29]. At higher diffraction orders, DEs of around 90% can be achieved when the GaP refractive index approaches the HRIL's. The case when the HRIL refractive index value equals the GaP refractive index ($n_{HRIL} = n_{GaP} = 3.04$) represents those situations too when the back surface of the crystal is microstructured (i.e., without using HRIL and ESR) and a metal layer is evaporated onto it, as shown in Fig. 1(a). We want to note that microstructuring the back surface of the semiconductor NM is more challenging than microstructuring a metal surface. Still, presumably, it is less challenging than microstructuring LN. (The Mohs hardness values of LN, GaP, and copper are 5.6 [30], 5 [31], and 3, respectively.)

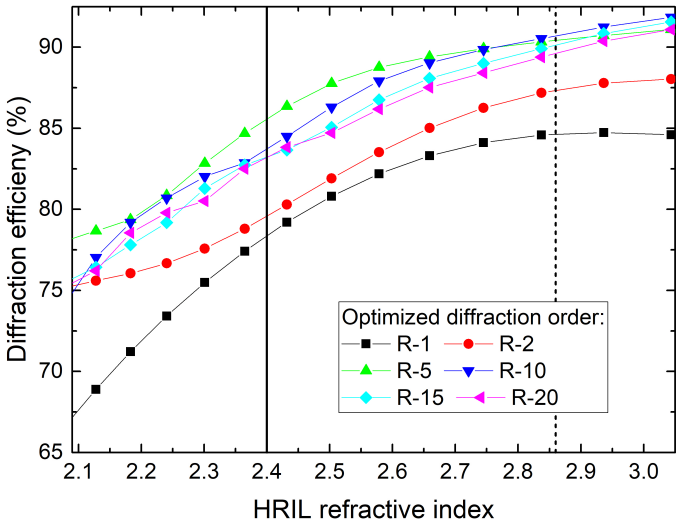

Fig. 2. The diffraction efficiency of the RNLS-ESR setup versus the HRIL refractive index for m = 1-20 diffraction orders. The points belonging to the highest HRIL refractive index value give back the case of the GaP-RNLS. The solid (dashed) vertical line represents the amorphous selenium (CS_2+MoS_2 HRIL) refractive index values.

One possibility to prepare HRIL is to disperse nanopowder into a relatively high refractive index liquid [32]. To our knowledge, the highest practically achievable HRIL refractive index is ~2.86 (see Fig. 2 dashed vertical line). In this case, the liquid is CS_2, and the nano powder is MoS_2. It is also possible to use amorphous selenium as the coupling material between the NM and the ESR. It has negligible absorption above ~1.5 μm, its refractive index is ~2.4 [33] (see Fig. 2 solid vertical line), and it has a low melting point of 50 C°. This possibility allows for a more straightforward implementation than the LN (LT) case, where the amorphous selenium

Optics EXPRESS

absorption of the high-intensity pump beam in the 1030 -800 nm range can lead to problems. The optical-to-THz conversion efficiencies will be discussed in Section 4.

3. GaP NLES

The nonlinear echelon slab (NLES) setup discussed in this Section is very similar to the one introduced in Ref. [16]. Similar to the case of the setup analyzed in Section 2, the change from LN to GaP can lead to significant advantages. In the case of GaP, owing to the significantly smaller pulse-front-tilt needed for the velocity matching, the slant angle (whose complementary angle is denoted by Φ in Fig. 3) of the volume phase holographic grating (VPHG) is also smaller. Thus, the technical implementation of the VPHG is significantly easier. Furthermore, presumably, the microstructuring of the GaP is also more accessible (see the Mohs hardness values above for LN and GaP). Another advantage of this setup is that, contrary to the one discussed in Section 2, there is no need for the application of HRIL. Furthermore, the pump and THz absorption is smaller (the pump is not propagating through the NM before THz generation, and there will be no residual free-carrier absorption). The disadvantage of the setup is that a VPHG has to be used before the microstructured NM.

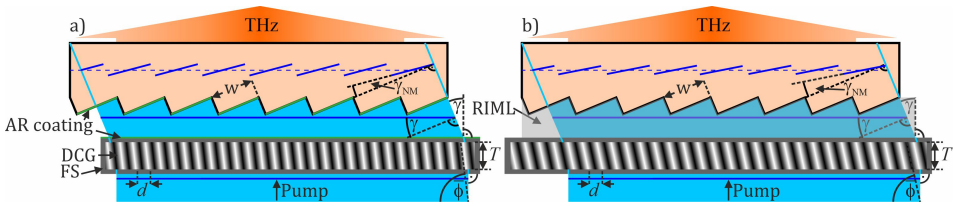

Fig. 3. GaP-NLES THz sources. (a) Air-spaced configuration with optional (AR) coating at the VPHG backside and the input facets of the echelon steps (green color). (b) RIML-filled configuration.

The simple and compact THz pulse source setup is shown in Fig. 3. The pump beam has normal incidence at the VPHG. Consequently, both the diffraction angle and the PFT angle can be equal to γ, and the pulse front is parallel to the plane of the VPHG. The pump beam enters the GaP-NLES at normal incidence to the input facets of the echelon steps (Fig. 3), whereby its propagation direction and average PFT angle remain unchanged. Inside the GaP, the pulse front becomes segmented [34] due to the discrete nature of the echelon steps. Furthermore, the tilt angle of the pulse-front segments will be smaller than the average tilt (because of the larger group index of GaP compared to air (Fig. 3(a)), or refractive index matching liquid (RIML) (Fig. 3(b))).

The local tilt angle of the individual pulse-front segments (Fig. 3) is determined by the following simple equation:

$$\tan(\gamma_{NM}) = \frac{n_g}{n_{g,NM}} \tan(\gamma). \tag{1}$$

Here, n_g is the group refractive index of the material filling the space between VPHG and NLES, and $n_{g,NM}$ is the group refractive index of NM. For efficient THz generation in the NM, an average PFT angle of $\gamma = 22.5°$ is needed at room temperature for 1.8 μm pump wavelength and 3 THz phase matching frequency. Figure 3(a) shows the most straightforward, air-spaced configuration ($n_g \approx 1$). In this case, it is useful to apply anti-reflection coating on the back side of the VPHG and the input facets of the echelon steps to reduce Fresnel losses. This coating is indicated by green in Fig. 3(a).

According to Eq. (1), the difference between the average and the local PFT angles can be reduced by RIML between the VPHG and the NLES. In such a RIML-filled configuration

Optics EXPRESS

Table 1. VPHG parameters of the three optimized designs.

Setup	Line density, $1/d$, (1/mm)	The thickness of the index-modulated layer, T (μm)	Slant angle, ϕ	DE (%)
Air-spaced	212.7	9.75	9.0°	76.01
BK7 RIML-filled	318.35	6.25	14.5°	91.9
Amorphous selenium-filled	425.2	5.5	22.5°	97.0

(Fig. 3(b)), the THz conversion efficiency and the bandwidth can be increased by reducing the dephasing related to pulse-front segmentation [16]. Furthermore, the RIML reduces Fresnel losses at the VPHG-liquid and liquid-GaP boundaries. The RIML can be a commercially available BK7 refractive index matching liquid or amorphous selenium. Here we would like to mention that the THz Fresnel loss at the output surface can be significantly reduced with an α-quartz plate of appropriate thickness or parylene AR coating [35].

The THz pulse propagates inside the NLES perpendicularly to the average PFT. The pulse leaves the NLES perpendicularly to its backside flat exit surface (Fig. 3). The duration of the initially Fourier-limited pump pulse will slightly increase, and its intensity will decrease behind the VPHG due to the angular dispersion and the associated group-velocity dispersion. However, the intensity is mainly affected by the diffraction of the individual pulse-front segments.

Numerical simulations were carried out by the COMSOL software to optimize the VPHGs parameters and to calculate the DE (including Fresnel losses) of the echelon structure. For the calculations, the average refractive index of the dichromated gelatin was 1.35, and the index

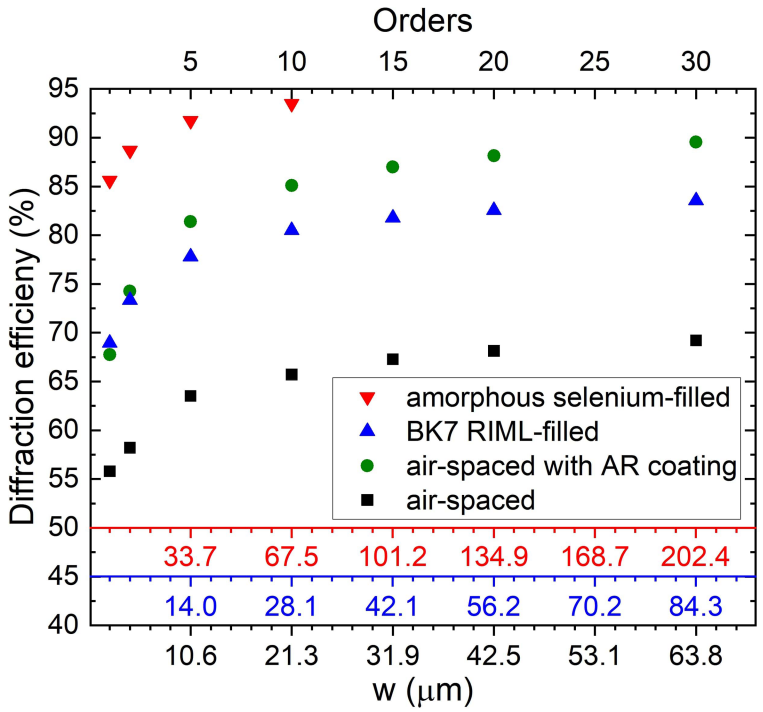

Fig. 4. Calculated pump DE belonging to the cases of air-spaced (black squares), air-spaced with AR coating (green circle), amorphous selenium-filled (red triangles), and the RIML filled (blue triangles). The first two setups are shown in Fig. 3(a), the other two in Fig. 3(b).

Optics EXPRESS

modulation was 0.15 [36]. In Table 1, the optimized parameters of the VPHG are shown. In the case of the air-spaced configuration, the VPHG diffraction angle is relatively small, leading to the reduced DE compared to the RIML-filled cases.

Figure 4 shows the diffraction efficiency of the microstructure belonging to the four investigated cases (amorphous selenium-filled, BK7 RIML-filled, air-spaced with AR coating, and air-spaced). As evident, the DE increases by increasing the order of diffraction exceeding the DE of the GaP CG and reaching the range comparable with the previously introduced GaP RNLS-ESR setup. Although applying AR coating provides higher DE than the BK7 RIML-filled case, the THz generation efficiency is affected by the deviation of the tilt angle of an individual pulse-front segment from the average pulse-front-tilt, which is significantly smaller for the RIML-filled case. THz generation efficiencies will be discussed in detail in Section 5.

4. Numerical model of THz generation

The basis of the numeric code can be found in Ref. [37]. The waveforms of the THz pulse and the pump pulse can be given as

$$E_{op}(t,z) = \mathcal{F}\left(A_{op}(\omega,z)\cdot e^{-ik(\omega)z}\right), \tag{2}$$

$$E_{THz}(t,z) = \mathcal{F}\left(A_{THz}(\omega,z)\cdot e^{-i\int_0^z \tilde{k}(z',\omega)dz'}\right), \tag{3}$$

where E is the electric field strength, $\mathcal{F}$ is the Fourier transform, k(ω) is the projection of the wave vector in the direction of the THz propagation, as in Ref. [37]. The two setups (GaP RNLS(-ESR) and GaP NLES) introduced above can be described by the same numerical model if the numerical modeling starts when the pump pulse starts to propagate upwards inside the NM (see Fig. 1 and 3). So in the case of GaP RNLS(ESR), the effects during the downward propagation and the diffraction/reflection at the NM's back surface will be considered separately. Similarly, in the case of GaP-NLES, the effects of the propagation through the VPHG, the air or RIML, and at the microstructured surface of the NM will be considered separately.

Different models have to be used when (a.) a fine microstructure is applied on the surface of the NM (low diffraction orders(s) are used) and when (b.) a rough microstructure is applied on the surface of the NM (high diffraction orders(s) are used). In the case of a.) a continuous tilted pulse front, while in the case of b.) a segmented tilted pulse front is created. Since, in semiconductors, the effect of free carriers generated by the multiphoton absorption of the pump pulse can be especially significant, (c.) the models have to consider this. All of the THz generation simulation results shown in Section 5 contain the Fresnel losses of the THz field. We want to mention again that this loss can be significantly reduced with an α-quartz plate or parylene AR coating.

4.1. Continuous tilted pulse front

The system of differential equations corresponding to the evolution of the THz field is:

$$\begin{aligned}\frac{dA_{THz}(\Omega,z)}{dz} &= -\frac{\alpha(\Omega,z)}{2}A_{THz}(\Omega,z)\\ &- i\frac{\Omega^2\chi^{(2)}_{eff}}{2c^2\tilde{k}(\Omega,z)}\int_0^\infty A_{op}(\omega+\Omega,z)A^*_{op}(\omega,z)\,e^{-i\left(k(\omega+\Omega)-k(\omega)-\tilde{k}(\Omega,z)\right)z}d\omega\end{aligned} \tag{4}$$

$$\begin{aligned}\frac{dA_{op}(\omega,z)}{dz} &= -i\frac{\Omega^2\chi^{(2)}_{eff}}{2c^2k(\omega)}\int_0^\infty A_{op}(\omega+\Omega,z)A^*_{THz}(\omega,z)e^{-i\left(k(\omega+\Omega)-k(\omega)-\tilde{k}(\Omega,z)\right)z}d\Omega\\ &- i\frac{\Omega^2\chi^{(2)}_{eff}}{2c^2k(\omega)}\int_0^\infty A_{op}(\omega-\Omega,z)A^*_{THz}(\omega,z)e^{-i\left(k(\omega-\Omega)-k(\omega)+\tilde{k}(\Omega,z)\right)z}d\Omega,\end{aligned} \tag{5}$$

taking into account the cascading effect as well.

Optics EXPRESS

4.2. Segmented tilted pulse front

The segmented nature of the pump pulse leads to two cardinal effects: The small beam waist of the beamlets [37,38] results in diffraction and inherently decreases the intensity. Therefore, in the 1D simulations, this effect was considered as the spatial dependent electric field strength of the pump, according to the following equation:

$$\begin{aligned}\frac{\mathrm{d}A_{op}(\omega,z)}{\mathrm{d}z} &= -\frac{5/4z^2+(ik(\omega)z-1)\left(z^2+z_R^2\right)}{\left(z+2ik(\omega)\left(z^2+z_R^2\right)\right)\left(z^2+z_R^2\right)}A(\omega,z)\\ &-i\frac{\Omega^2\chi_{eff}^{(2)}}{2c^2k(\omega)}\int_0^\infty A_{op}(\omega+\Omega,z)A_{THz}^*(\omega,z)e^{-i\left(k(\omega+\Omega)-k(\omega)-\tilde{k}(\Omega,z)\right)z}d\Omega\\ &-i\frac{\Omega^2\chi_{eff}^{(2)}}{2c^2k(\omega)}\int_0^\infty A_{op}(\omega-\Omega,z)A_{THz}^*(\omega,z)e^{-i\left(k(\omega-\Omega)-k(\omega)+\tilde{k}(\Omega,z)\right)z}d\Omega.\end{aligned} \tag{6}$$

The parameter z_R in the equation is the Rayleigh length of the Gaussian beam, where the beam waist is $d/(2\cos(\gamma))$ (see Fig. 1). In the appendix, there is a more detailed explanation of the first term of Eq. (6).

The other substantial effect is that the generated THz pulse interacts with more and more beamlets along its propagation. When solving the system of differential Eqs. (4) and (6), one should not forget that the tilt angle of a given beamlet is not harmonious with the velocity matching. Therefore, the group velocity of the beamlet is larger than the velocity of the THz pulse. However, when the THz pulse reaches the edge of the beamlet and jumps into the neighboring beamlet, the group delay of the pump changes. The model considers this effect by resetting the group delay of the pump as the pump moves from beamlet to beamlet.

4.3. Effect of multiphoton absorption

During the propagation, the index of refraction in the THz range is not constant but varies according to

$$n_{THz}(\Omega,z) = \Re\left(\sqrt{\varepsilon_{r0}(\Omega)+\varepsilon_{fc}(\Omega,z)}\right) \tag{7}$$

due to the free charge carriers induced by the multiphoton absorption process of the pump pulse. This effect is taken into account in $\tilde{k}(z,\omega)$, when calculating the THz field in Eq. (2). In Eq. (7) $\varepsilon_{r0}(\Omega)$ is the dielectric permittivity of the material without the free carriers [39]. The permittivity attributed to the free carriers can be described with the following equation:

$$\varepsilon_{fc}(\Omega,z) = -\frac{q^2}{\varepsilon_0 m_{eff}}\frac{N_{wa}(z)}{\Omega^2+i\Omega/\tau_{sc}}, \tag{8}$$

where q is the charge of the electron, ε_0 is the vacuum permittivity, m_{eff} is the effective mass of the electron, τ_{sc} is the electron scattering time, $N_{wa}(z)$ is the weighted average of the free carrier density in the z point, which was defined according to the followings:

$$N_{wa}(z) = \frac{\int_{-\infty}^{\infty}A_{THz}^2(t,z)N_c(z,t)\mathrm{d}t}{\int_{-\infty}^{\infty}A_{THz}^2(t,z)\mathrm{d}t}, \tag{9}$$

$$N_c(z,t) = \frac{\beta_4}{4h\nu_0}\int_{-\infty}^{t}I_{op}^4(t',z)\mathrm{d}t', \tag{10}$$

where $\beta_4 = 2.6\times10^{-4}\mathrm{cm}^5\mathrm{GW}^{-3}$ [25] is the four-photon absorption coefficient of GaP, h is the Planck constant, ν_0 is the central pump frequency and $I_{op}(t,z)$ is the temporal intensity in the z

Optics EXPRESS

point. The THz absorption coefficient can be determined from the permittivity as

$$\alpha(\Omega, z) = 2\frac{\Omega}{c}\Im\left(\sqrt{\varepsilon_{r0}(\Omega) + \varepsilon_{fc}(\Omega, z)}\right). \tag{11}$$

Here we would like to note that in several papers, the contribution of the induced free carriers to the THz absorption was incorrectly expressed [10,40–42].

5. THz simulation results

Terahertz generation efficiencies were calculated for the GaP NLES BK7 RIML-filled configuration, pumped at 1800 nm pump wavelength and 100 fs pulse duration, where the four-photon absorption is the lowest order multiphoton absorption process. The optical-to-THz generation efficiency dependence on the pump intensity is shown in Fig. 5 for four different w step sizes of the microstructured surface (see Fig. 3(b)). In the case of Fig. 5(a), the height of the microstructure is so small that the tilted pulse front can be considered as a continuous one. The pulse front tilting was segmented in the other cases (Fig. 5(b)-d). Here we want to note that the continuous pulse front case (Fig. 5(a)) also describes the GaP RNLS(ESR) setup up to the ~20th order (amorphous selenium as HRIL case) if the free carriers generated by the pump pulse propagating to the back side of the crystal is omitted. In general, it can be said that the pulse front can be considered continuous if the structure height is smaller than the quarter of the spatial pulse length.

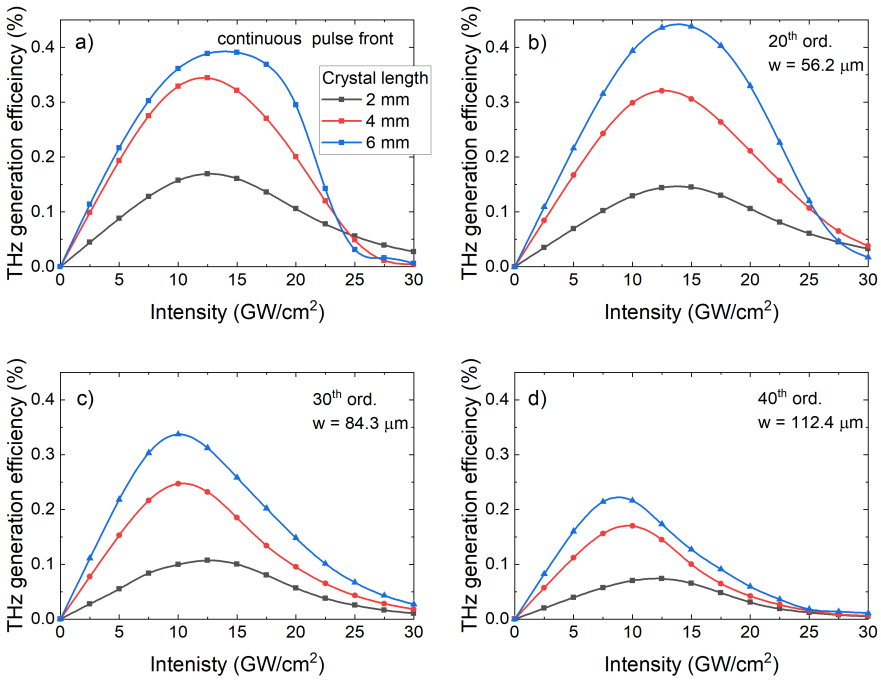

Fig. 5. Intensity-dependent THz generation efficiency at three different crystal lengths (different colors) for the microstructured surface's four different step sizes (w, see Fig. 3(b)). The tilted pump pulse front was continuous (a) and segmented (b-d).

At optimal step size (w= 56.2 μm), the THz-generation efficiency is slightly better than when using a diffraction grating. If the size of the microstructure is too big, the effect of the $\gamma_{NM} \neq \gamma$ tilt angle of the individual beamlets becomes significant and the THz-generation efficiency will not increase monotonic with the crystal length. Still, a periodically modulated curve can be

Optics EXPRESS

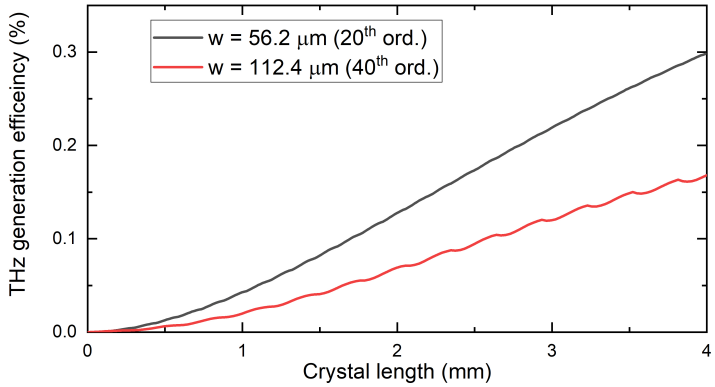

Fig. 6. Terahertz generation efficiency along the crystal length in the case of 56.2 μm (black) and 112.4 μm (red) stair step size. The intensity was optimal for both step sizes.

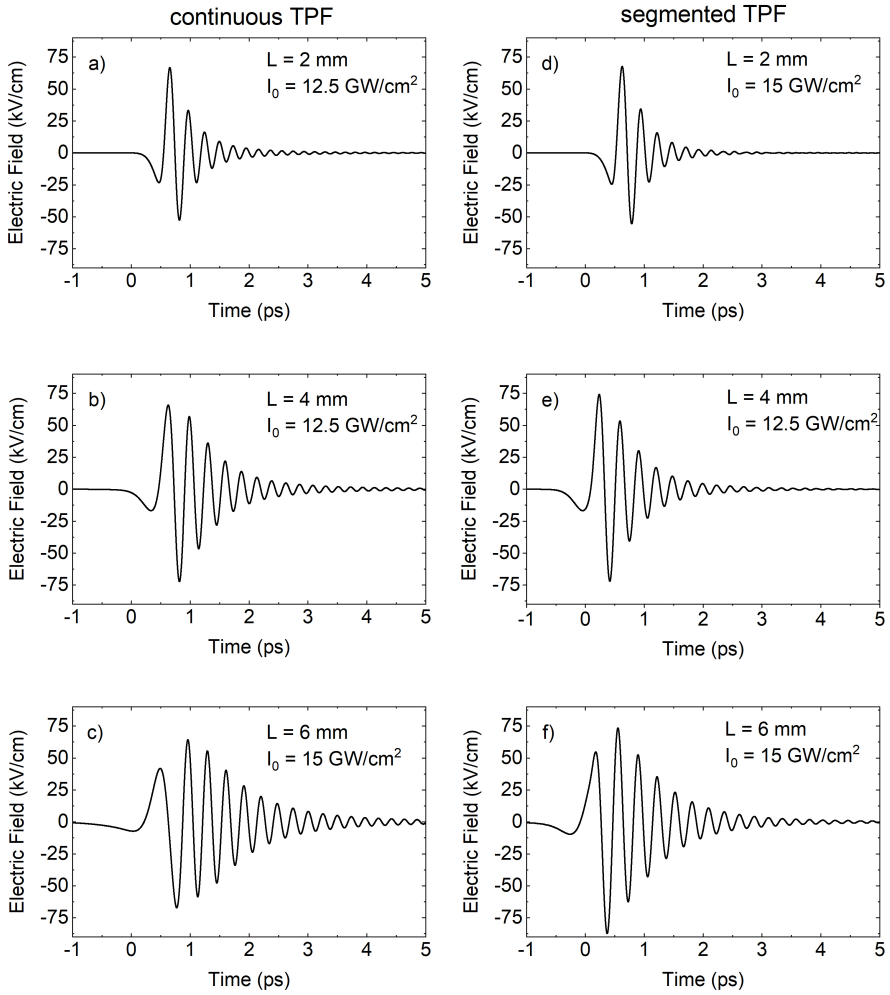

Fig. 7. THz pulse shapes in the case of continuous (a-c) and segmented (d-f) pulse front. The chosen pump intensities correspond to the highest efficiencies in Fig. 5(a) and (b).

Optics EXPRESS

observed with a smaller average slope. This effect is shown in Fig. 6, where the THz generation efficiency was depicted along the crystal length.

Figure 7(a-f) shows the THz pulse shapes in the case of continuous (a-c) and segmented (d-f) tilted pulse fronts. The microstructured surface's intensities and the step size were chosen according to the highest efficiencies in Fig. 5. (a-b). It can be seen that contrary to the conversion efficiency, the peak electric field is almost independent of the crystal length (for longer than 2 mm crystal length). The material dispersion in the THz range is responsible for this behavior. For longer crystals, the THz pulse becomes longer, containing more oscillations and energy, but the peak field strength remains nearly constant. Up to a crystal length of 4 mm, the second peak remains smaller than the main peak, and the pulse shape can be considered nearly single-cycle. It means that GaP-NLES can generate nearly single-cycle THz pulses with ~0.4% efficiency (see Fig. 5(a),b). The peak electric fields are 66 and 74 kV/cm for the continuous and segmented pulse fronts in the case of a 4 mm crystal. Supposing a 2 inch diameter crystal size and a 3-inch off-axis parabolic mirror, the pulses can be tightly focused, and 15.2 MV/cm and 17 MV/cm peak electric field can be achieved, respectively.

6. Discussion

In the case of the GaP NLES setup, more than 0.4% THz generation efficiencies can be achieved. In this case, the crystal length is 6 mm, and the THz pulse is chirped. If the goal is to generate near single-cycle THz pulses, the crystal thickness should not be larger than 4 mm. In this case, the THz generation efficiency is ~0.3% which approaches the efficiency of the LN-based setups. A significant disadvantage of the RNLS against the NLES setups is that in the case of the RNLS, the THz generation occurs when the pump has already passed through one time the NM crystal and created free carriers. Therefore, the THz absorption of the crystal is significantly higher in the case of RNLS than in the case of NLES. According to the calculations, the efficiency of RNLS is ~2 times smaller than in the case of NLES. We emphasize that the significant multiphoton absorption causes this disadvantage, occurring even at relatively low intensities (at 10 GW/cm^2). This disadvantage does not appear if the multiphoton absorption is much lower than in the investigated case; for example, if the NM is LN [16], or the semiconductor is pumped at a longer wavelength.

7. Conclusion

Efficient and scalable THz pulse sources based on optical rectification in microstructured semiconductors are proposed and investigated for GaP NM. In the case of GaP-RNLS(-ESR), the pulse-front tilt is introduced by a periodic structure created on the back surface of the NM (or a nearby metal plate). In the GaP-NLES setup, it is introduced by a VPHG. Both setups can have a higher pump to THz conversion efficiency than the CG setup because it is not limited by the co-propagating and interfering $\pm m^{th}$ diffraction orders. Furthermore, both setups can have ~10% higher diffraction efficiency than the CG setup. The implementation of the GaP RNLS ESR, using amorphous selenium between the ESR and the NM, can be significantly easier than using nanocomposite liquids as HRIL. In this case, only a metal plate has to be microstructured, which is considerably more accessible and precise than microstructuring an NM surface. Simulation results suggest that nearly single-cycle THz pulses can be generated in a 4 mm thick crystal with 0.4% conversion efficiency in the GaP-NLES BK7 RIML-filled setup. These results do not suppose AR coating for the generated THz pulses. Supposing 20 mJ pump energy 17 MV/cm focused (by an off-axis parabolic mirror) peak THz electric field can be expected by the GaP-NLES BK7 RIML-filled setup.

Optics EXPRESS

Appendix

Our goal is to construct a differential equation that has a solution for the electric field strength in the form of

$$E(z) = \frac{E_0}{\sqrt[4]{1+\frac{z^2}{z_R^2}}} \exp(-ikz). \tag{12}$$

The reason for using the fourth root in the denominator (instead of the square root used for Gaussian beams) is that we are going to describe beams having an elliptic beam profile with eccentricity very close to 1 (larger than 0.999).

In the frequency domain, the 1D linear wave equation reads as:

$$\frac{\partial^2}{\partial z^2} E(\omega, z) + k^2(\omega) E(\omega, z) = 0. \tag{13}$$

The plane waves are the solution of Eq. (13), but not the Gaussian beam. Nonetheless, we are looking for a solution to Eq. (13) in the following form:

$$E(\omega, z) = \frac{E_0}{\sqrt[4]{1+\frac{z^2}{z_R^2}}} \breve{A}(\omega, z) \exp(-ikz), \tag{14}$$

where $z_R = \frac{1}{2}k(\omega)w_0^2$ is the Rayleigh length. Substituting Eq. (14) into Eq. (13), performing the second-order derivation, and introducing the $q = \sqrt[4]{1+\frac{z^2}{z_R^2}}$ notation, we obtain:

$$\left[\frac{5z^2}{4z_R^4 q^9} + \frac{ikz}{z_R^2 q^5}\right] \breve{A}(\omega, z) - \left[\frac{z}{z_R^2 q^5} + \frac{2ik}{q}\right] \frac{\partial}{\partial z} \breve{A}(\omega, z) + \frac{1}{q} \frac{\partial^2}{\partial z^2} \breve{A}(\omega, z) = 0. \tag{15}$$

Assuming slowly varying envelope approximation and omitting the second derivative, our differential equation can be written in the following form:

$$\frac{\partial}{\partial z} \breve{A}(\omega, z) = \frac{5/4z^2 + (ik(\omega)z - 1)\left(z^2 + z_R^2\right)}{\left(z + 2ik(\omega)\left(z^2 + z_R^2\right)\right)\left(z^2 + z_R^2\right)} \breve{A}(\omega, z). \tag{16}$$

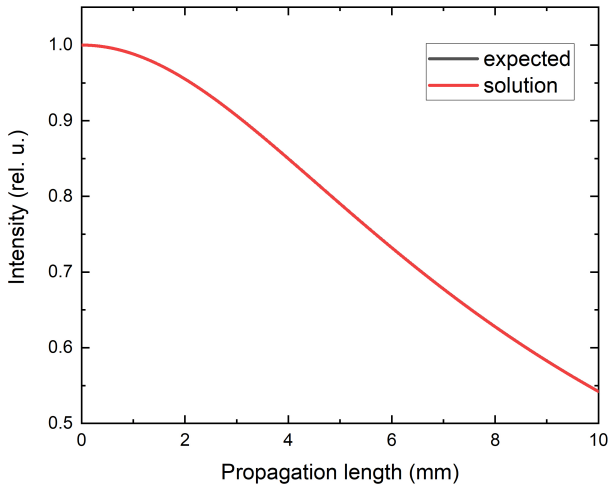

Fig. 8. Relative intensity according to Eq. (14) (black) and the solution of Eq. (17) differential equation (red).

Optics EXPRESS

Since the solution of Eq. (13) is a plane wave, $A(\omega, z)$ has to vary in such a way that satisfy the plane-wave equation in the form of Eq. (14). If we expect the electric field strength to vary as a Gaussian beam, the term obtained from Eq. (16) has to be applied, but with opposite sign:

$$\frac{\partial}{\partial z}\breve{A}(\omega, z) = -\frac{5/4z^2 + (ik(\omega)z - 1)\left(z^2 + z_R^2\right)}{\left(z + 2ik(\omega)\left(z^2 + z_R^2\right)\right)\left(z^2 + z_R^2\right)}\breve{A}(\omega, z), \tag{17}$$

where $A(\omega, z)$ is the electric field envelope which was defined as A_{op} in Eq. (2). Figure 8 shows the dependence of the pump intensity on the propagation length according to Eq. (14) and the solution of Eq. (17), respectively. As can be seen, the two curves are the same.

Funding. National Research, Development and Innovation Office (2018-1.2.1-NKP-2018-00009, 2018-1.2.1-NKP-2018-00010, TKP2020-IKA-08); Hungarian Scientific Research Fund (OTKA) (129134).

Acknowledgments. Gergő Krizsán acknowledges support from the ÚNKP-21-4 New National Excellence Program of the Ministry for Innovation and Technology from the source of the National Research, Development, and Innovation Office. In addition, Zoltán Tibai and György Tóth would like to thank the support of the János Bolyai Research Scholarship of the Hungarian Academy of Science.

Disclosures. The authors declare no conflicts of interest.

Data availability. Data underlying the results presented in this paper are not publicly available at this time but may be obtained from the authors upon reasonable request.

References

1. S. Schlauderer, C. Lange, S. Baierl, T. Ebnet, C. P. Schmid, D. C. Valovcin, A. K. Zvezdin, A. V. Kimel, R. V. Mikhaylovskiy, and R. Huber, "Temporal and spectral fingerprints of ultrafast all-coherent spin switching," Nature **569**(7756), 383–387 (2019).
2. J. Lu, Y. Zhang, H. Y. Hwang, B. K. Ofori-Okai, S. Fleischer, and K. A. Nelson, "Nonlinear two-dimensional terahertz photon echo and rotational spectroscopy in the gas phase," Proc. Natl. Acad. Sci. **113**(42), 11800–11805 (2016).
3. S. F. Maehrlein, I. Radu, P. Maldonado, A. Paarmann, M. Gensch, A. M. Kalashnikova, R. V. Pisarev, M. Wolf, P. M. Oppeneer, J. Barker, and T. Kampfrath, "Dissecting spin-phonon equilibration in ferrimagnetic insulators by ultrafast lattice excitation," Sci. Adv. **4**(7), eaar5164 (2018).
4. V. Balos, G. Bierhance, M. Wolf, and M. Sajadi, "Terahertz-magnetic-field induced ultrafast faraday rotation of molecular liquids," Phys. Rev. Lett. **124**(9), 093201 (2020).
5. P. Salén, M. Basini, S. Bonetti, J. Hebling, M. Krasilnikov, A. Y. Nikitin, G. Shamuilov, Z. Tibai, V. Zhaunerchyk, and V. Goryashko, "Matter manipulation with extreme terahertz light: Progress in the enabling thz technology," Phys. Rep. **836-837**, 1–74 (2019).
6. S. Turnár, J. Hebling, J. A. Fülöp, G. Tóth, G. Almási, and Z. Tibai, "Design of a thz-driven compact relativistic electron source," Appl. Phys. B **127**(3), 38 (2021).
7. D. Zhang, A. Fallahi, M. Hemmer, X. Wu, M. Fakhari, Y. Hua, H. Cankaya, A.-L. Calendron, L. E. Zapata, N. H. Matlis, and F. X. Kärtner, "Segmented terahertz electron accelerator and manipulator (steam)," Nat. Photonics **12**(6), 336–342 (2018).
8. L. Pálfalvi, J. A. Fülöp, G. Tóth, and J. Hebling, "Evanescent-wave proton postaccelerator driven by intense thz pulse," Phys. Rev. Spec. Top.–Accel. Beams **17**(3), 031301 (2014).
9. B. Zhang, Z. Ma, J. Ma, X. Wu, C. Ouyang, D. Kong, T. Hong, X. Wang, P. Yang, L. Chen, Y. Li, and J. Zhang, "1.4-mj high energy terahertz radiation from lithium niobates," Laser Photonics Rev. **15**(3), 2000295 (2021).
10. J. A. Fülöp, L. Pálfalvi, G. Almási, and J. Hebling, "Design of high-energy terahertz sources based on optical rectification," Opt. Express **18**(12), 12311–12327 (2010).
11. L. Tokodi, J. Hebling, and L. Pálfalvi, "Optimization of the tilted-pulse-front terahertz excitation setup containing telescope," J. Infrared, Millimeter, Terahertz Waves **38**(1), 22–32 (2017).
12. G. Tóth, L. Pálfalvi, J. A. Fülöp, G. Krizsán, N. H. Matlis, G. Almási, and J. Hebling, "Numerical investigation of imaging-free terahertz generation setup using segmented tilted-pulse-front excitation," Opt. Express **27**(5), 7762–7775 (2019).
13. Z. Ollmann, J. Hebling, and G. Almási, "Design of a contact grating setup for mj-energy thz pulse generation by optical rectification," Appl. Phys. B **108**(4), 821–826 (2012).
14. M. Tsubouchi, K. Nagashima, F. Yoshida, Y. Ochi, and M. Maruyama, "Contact grating device with fabry-perot resonator for effective terahertz light generation," Opt. Lett. **39**(18), 5439–5442 (2014).
15. L. Pálfalvi, Z. Ollmann, L. Tokodi, and J. Hebling, "Hybrid tilted-pulse-front excitation scheme for efficient generation of high-energy terahertz pulses," Opt. Express **24**(8), 8156–8169 (2016).
16. G. Krizsán, Z. Tibai, G. Tóth, P. S. Nugraha, G. Almási, J. Hebling, and J. A. Fülöp, "Uniformly scalable lithium niobate thz pulse source in transmission geometry," Opt. Express **30**(3), 4434–4443 (2022).

Optics EXPRESS

17. G. Tóth, L. Pálfalvi, Z. Tibai, L. Tokodi, J. A. Fülöp, Z. Márton, G. Almási, and J. Hebling, "Single-cycle scalable terahertz pulse source in reflection geometry," Opt. Express **27**(21), 30681–30691 (2019).
18. G. Krizsán, Z. Tibai, J. Hebling, L. Pálfalvi, G. Almási, and G. Tóth, "Lithium niobate and lithium tantalate based scalable terahertz pulse sources in reflection geometry," Opt. Express **28**(23), 34320–34327 (2020).
19. G. Polónyi, B. Monoszlai, G. Gäumann, E. J. Rohwer, G. Andriukaitis, T. Balciunas, A. Pugzlys, A. Baltuska, T. Feurer, J. Hebling, and J. A. Fülöp, "High-energy terahertz pulses from semiconductors pumped beyond the three-photon absorption edge," Opt. Express **24**(21), 23872–23882 (2016).
20. J. A. Fülöp, G. Polónyi, B. Monoszlai, G. Andriukaitis, T. Balciunas, A. Pugzlys, G. Arthur, A. Baltuska, and J. Hebling, "Highly efficient scalable monolithic semiconductor terahertz pulse source," Optica **3**(10), 1075–1078 (2016).
21. M. Bashirpour, W. Cui, A. Gamouras, and J.-M. Ménard, "Scalable fabrication of nanogratings on gap for efficient diffraction of near-infrared pulses and enhanced terahertz generation by optical rectification," Crystals **12**(5), 684 (2022).
22. W. Cui, K. M. Awan, R. Huber, K. Dolgaleva, and J.-M. Ménard, "Broadband and high-sensitivity time-resolved THz system using grating-assisted tilted-pulse-front phase matching," Adv. Opt. Mater. **10**(1), 2101136 (2021).
23. J. Hebling, K.-L. Yeh, M. C. Hoffmann, B. Bartal, and K. A. Nelson, "Generation of high-power terahertz pulses by tilted-pulse-front excitation and their application possibilities," J. Opt. Soc. Am. B **25**(7), B6–B19 (2008).
24. J. Hebling, A. G. Stepanov, G. Almási, B. Bartal, and J. Kuhl, "Tunable thz pulse generation by optical rectification of ultrashort laser pulses with tilted pulse fronts," Appl. Phys. B **78**(5), 593–599 (2004).
25. M. I. Bakunov and S. B. Bodrov, "Terahertz generation with tilted-front laser pulses in a contact-grating scheme," J. Opt. Soc. Am. B **31**(11), 2549–2557 (2014).
26. B. Monoszlai, P. S. Nugraha, G. Tóth, G. Polónyi, L. Pálfalvi, L. Nasi, Z. Ollmann, E. J. Rohwer, G. Gäumann, J. Hebling, T. Feurer, and J. A. Fülöp, "Measurement of four-photon absorption in gap and znte semiconductors," Opt. Express **28**(8), 12352–12362 (2020).
27. C. L. Davies, J. B. Patel, C. Q. Xia, L. M. Herz, and M. B. Johnston, "Temperature-dependent refractive index of quartz at terahertz frequencies," J. Infrared, Millimeter, Terahertz Waves **39**(12), 1236–1248 (2018).
28. G. Ghosh, "Dispersion-equation coefficients for the refractive index and birefringence of calcite and quartz crystals," Opt. Commun. **163**(1-3), 95–102 (1999).
29. Z. Ollmann, J. Fülöp, J. Hebling, and G. Almási, "Design of a high-energy terahertz pulse source based on znte contact grating," Opt. Commun. **315**, 159–163 (2014).
30. K. G. Subhadra, K. K. Rao, and D. B. Sirdeshmukh, "Systematic hardness studies on lithium niobate crystals," Bull. Mater. Sci. **23**(2), 147–150 (2000).
31. P. B. Hart, *Gallium Phosphide* (Palgrave Macmillan UK, 1971), pp. 147–154.
32. M. Trikeriotis, R. Rodriguez, M. F. Zettel, A. Bakandritsos, W. J. Bae, P. A. Zimmerman, C. K. Ober, and E. P. Giannelis, "High refractive index nanoparticle fluids for 193-nm immersion lithography," in *Advances in Resist Materials and Processing Technology XXVI*, C. L. Henderson, ed. (SPIE, 2009).
33. A. Solieman and A. Abu-Sehly, "Modelling of optical properties of amorphous selenium thin films," Phys. B **405**(4), 1101–1107 (2010).
34. L. Pálfalvi, G. Tóth, L. Tokodi, Z. Márton, J. A. Fülöp, G. Almási, and J. Hebling, "Numerical investigation of a scalable setup for efficient terahertz generation using a segmented tilted-pulse-front excitation," Opt. Express **25**(24), 29560–29573 (2017).
35. M. Ji, C. Musante, S. Yngvesson, A. Gatesman, and J. Waldman, "Study of parylene as anti-reflection coating for silicon optics at thz frequencies," in *Proceedings of the Eleventh International Symposium on Space Terahertz Technology* (University of Michigan Solid-State Electronics Laboratory, Ann Arbor, MI, 2000).
36. I. K. Baldry, J. Bland-Hawthorn, and J. G. Robertson, "Volume phase holographic gratings: Polarization properties and diffraction efficiency," Publ. Astron. Soc. Pac. **116**(819), 403–414 (2004).
37. K. Ravi, W. R. Huang, S. Carbajo, X. Wu, and F. Kärtner, "Limitations to thz generation by optical rectification using tilted pulse fronts," Opt. Express **22**(17), 20239–20251 (2014).
38. L. Wang, T. Kroh, N. H. Matlis, and F. Kärtner, "Full 3d+1 modeling of tilted-pulse-front setups for single-cycle terahertz generation," J. Opt. Soc. Am. B **37**(4), 1000–1007 (2020).
39. D. F. Parsons and P. D. Coleman, "Far infrared optical constants of gallium phosphide," Appl. Opt. **10**(7), 1683_1 (1971).
40. S.-C. Zhong, Z.-H. Zhai, J. Li, L.-G. Zhu, J. Li, K. Meng, Q. Liu, L.-H. Du, J.-H. Zhao, and Z.-R. Li, "Optimization of terahertz generation from $linbo_3$ under intense laser excitation with the effect of three-photon absorption," Opt. Express **23**(24), 31313–31323 (2015).
41. G. Polónyi, M. I. Mechler, J. Hebling, and J. A. Fülöp, "Prospects of semiconductor terahertz pulse sources," IEEE J. Sel. Top. Quantum Electron. **23**(4), 1–8 (2017).
42. P. S. Nugraha, G. Krizsán, G. Polónyi, M. I. Mechler, J. Hebling, G. Tóth, and J. A. Fülöp, "Efficient semiconductor multicycle terahertz pulse source," J. Phys. B: At., Mol. Opt. Phys. **51**(9), 094007 (2018).